Case Studies in Nondestructive Testing and Evaluation 6 (2016) 1–7

Contents lists available at ScienceDirect

Case Studies in Nondestructive Testing and Evaluation

www.elsevier.com/locate/csndt

Characterization of pearls by X-ray phase contrast imaging with a grating interferometer

Vincent Revol [a,*], Carina Hanser [b], Michael Krzemnicki [b]

[a] CSEM SA, Untere Gründlistrasse 1, 6055 Alpnach Dorf, Switzerland
[b] SSEF Schweizerisches Gemmologisches Institut, Aeschengraben 26, 4051 Basel, Switzerland

ARTICLE INFO

Article history:
Available online 8 June 2016

ABSTRACT

In this study, X-ray phase contrast imaging with a grating interferometer is applied on pearls for the first time in order to distinguish natural pearls from cultured pearls. Traditionally, this separation is mainly based on X-ray radiography. In order to visualize the internal structure of pearls we used a custom-made grating interferometer setup and performed measurements on three different pearl products, a natural pearl, a beaded cultured pearl and a beadless cultured pearl. To enhance the visibility of the internal pearl structures, we applied a high-pass filter in order to better conclude on the applicability of this technique to the separation of natural and cultured pearls. The study shows that it is possible to visualize internal pearl structures using distinctly shorter exposure times compared to traditional X-ray radiography and that X-ray phase contrast imaging is a promising complementary method for pearl analysis.

1. Introduction

One of the major issues in the international pearl trade is the reliable separation of natural pearls from cultured ones. Natural pearls accidentally form in a wild mollusc without any human intervention, whereas cultured pearls result from a grafting operation in certain mollusc species (e.g. *Pinctada maxima, Pinctada margaritifera, Unio*) [1–4]. Generally, there is an important price gap between these two products in the trade. In 2011, the Peregrina pearl, a historical natural pearl of exceptional size and quality, was sold for US$ 11 mio at auction, whereas cultured pearls of low quality may just cost a few cents [5].

The trade relies on specialized gemmological laboratories to identify pearls and to distinguish natural from cultured pearls. This separation requires a detailed analysis of the pearl's internal structure, such as the presence, concentration and orientation of organic matter within the calcium carbonate matrix. Based on this analysis, it is possible to trace back the natural or cultured formation of a pearl. Few non-destructive techniques are capable of achieving a sufficient level of details to perform an efficient separation. Most commonly, pearl testing is performed using X-ray film techniques [2,6]. The method is, however, time-consuming and requires the use of chemicals. X-ray digital radiography is still confronted with technical challenges such as the sensitivity, dynamic range and resolution of detectors – in particular because of the spherical shape of the pearl. The variable path lengths within the pearl lead to strong variations of the X-ray intensity on the detector.

* Corresponding author. Tel.: +41 41 672 7533, fax: +41 41 672 7500.
E-mail address: vincent.revol@csem.ch (V. Revol).

http://dx.doi.org/10.1016/j.csndt.2016.06.001

Fig. 1. (From left to right): saltwater natural pearl (NP-2f), beaded saltwater cultured pearl (CP-2f) and beadless freshwater cultured pearl (CP-1b).

The use of an immersion liquid with matching X-ray attenuation helps to reduce these artefacts but cannot avoid them. Moreover, the usual matching liquids are difficult to handle as a result of their toxicity.

In recent years, digital X-ray micro-tomography (µCT) has been introduced to visualize the internal structure of a pearl in three dimensions (3D). Indeed, pearls do not only consist of $CaCO_3$ but also of organic layers which can be distinguished because of their differing X-ray densities. Similarly, beads and cavities can be detected [7,8]. Although µCT allows a better evaluation of the orientation of such features compared to X-ray radiography, it requires long exposure times (from 30 to 120 minutes) and generates large data sets, which renders the data analysis complex and time-consuming. There is thus a need for novel non-destructive techniques, capable of revealing the internal structure with short measurement times.

Within this collaboration, we have investigated the potential of using grating-based X-ray phase contrast imaging for the characterization of pearls. The technology has initially been developed using synchrotron light [9,10] and was later on extended to be usable with standard X-ray tube sources [11]. Recently, technical improvements on the design of X-ray interferometers allowed to extend the use of this technique toward industrial applications by enlarging the size of the field of view and the usable X-ray energies [12–14].

We report here on the analysis of X pearl samples of different types and discuss the applicability of the method for detection of natural versus cultured pearls.

2. Materials and methods

2.1. Test specimen

For this study, we selected three pearl samples representing the three main pearl types according to their formation: a natural pearl, a beaded cultured pearl and beadless cultured pearl (Fig. 1).

- NP-2f is a small, slightly drop-shaped saltwater natural pearl of cream colour from Pinctada radiata and originates from the Arabian Gulf in Bahrain.
- CP-2f is a large, round, beaded saltwater cultured pearl from Pinctada margaritifera. It is brownish to brownish-grey in colour, shows irregular surface structures and originates from Tahiti.
- CP-1b is a white, button-shaped beadless freshwater cultured pearl from Hyriopsis cumingii and was produced in China.

2.2. Grating interferometer

The grating interferometer used for the experiments consists of the combination of a commercial X-ray source tube (Varian HPX160-20, focal spot 0.4×0.4 mm^2), a commercial X-ray detector (Dexela DEX2315, pixel size 75 µm, resolution 3072×1944) and three custom-made X-ray gratings. A schematic view of the setup is displayed in Fig. 2.

The three gratings were produced in the clean rooms of CSEM in Neuchâtel, Switzerland using silicon wafers with a diameter of 150 mm. The phase grating G1 was made out of silicon by wet etching while G0 and G2 are absorption gratings obtained by gold deposition on a structured silicon substrate. The periods p_0, p_1 and p_2 of the three gratings G0, G1 and G2 were equal to 20 µm, 3.333 µm and 4 µm respectively, while the depths were equal to 100 µm, 25.77 µm and 100 µm respectively. The depth of the grating G1 made out of silicon corresponds to a phase shift of $\pi/2$ for the design X-ray energy of $E_d = 40$ keV. The distance between gratings G0 and G1 was 1075 mm and between G1 and G2, 215 mm. Because of the magnification of 1.3 used here, the intrinsic resolution in the sample was equal to 57.7 µm.

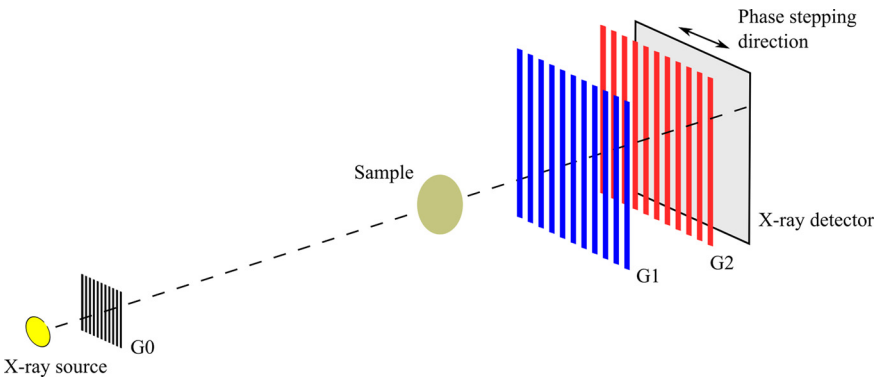

Fig. 2. Schematic view of the Talbot–Lau grating interferometer, where the sample is placed between the gratings G0 and G1.

2.3. Image processing and fusion

The principle of grating interferometry is described in details in the literature [13,15]. The images were reconstructed with help of the phase stepping approach using the translation of the grating G2 [16]. From the recorded intensity signal, three complementary images were reconstructed (see [13] for more details on the reconstruction method), namely the absorption image, the differential phase contrast image and the scatter dark field image (see Fig. 3).

The absorption image is similar to the image acquired with a standard X-ray industrial system (without gratings) and is proportional to the absorption coefficient times the thickness of the material. The differential phase contrast image is related to the refraction angle, whereas the scatter dark field image is equal to the ultra-small angle X-ray scattering coefficient times the thickness of the material. The ultra-small angle X-ray scattering is linked to variations of the electronic density at the microscopic level [14,17]. The scatter dark field image provides insights into the inhomogeneity of the sample below the pixel resolution such as micro-gaps, porosity etc.

For the measurements, we used an acceleration voltage of 60 kVp and an anode current of 10 mA. The number of phase steps was equal to 49 while the exposure time of a single image was set to 800 ms. The procedure was repeated 5 times and the obtained images were averaged, which results in a total acquisition time of about 200 s.

The inspection of pearls is based on the analysis of fine structures within the pearls, meaning that the high frequencies in the image are relevant. A bandpass filter was used to filter out structures larger than 10 pixels (equivalent to 577 µm) in order to emphasize the high frequency and to allow a qualitative comparison of the absorption, differential phase contrast and scatter dark field images. For this purpose, we used the built-in function of ImageJ (. . . /Process/FFT/Bandpass filter) [18]. The filter was applied to all three images in a similar manner.

3. Results

The results obtained for three different pearls are summarized in this section. Fig. 3 shows the images obtained for pearl NP-2f. This natural pearl shows a characteristic onion-like internal structure consisting of an organic-rich centre followed by alternating calcium carbonate-rich and organic-rich layers. The main alternating layers are well discernible in all images. One layer is indicated by the red arrows in Fig. 3. However, the organic-rich (with microfissures) centre point of the pearl (yellow arrow) and the presence of cracks in the external layer (blue arrow) can only be seen in the dark field image. As expected, the application of the high pass filter helps to visualize the key features such as the layers in Fig. 3-d and the cracks in Fig. 3-f.

Fig. 4 shows the images obtained on pearl CP-2f. This saltwater cultured pearl consists of a thin layer of nacre deposited onto a spherical seeding bead. Some irregular surface structures can be seen at the top of all images. The interface layer between the nacre and the bead is thin and cannot be recognized in some parts of the pearl using the absorption and differential phase contrast images (Fig. 4-ab). Even after applying the high pass filter, some parts of the interface layer stay invisible. The interface can however be well detected using the scatter dark field image (Fig. 4-cf). The ability to clearly visualize the spherical shape of the bead facilitates the classification of this pearl as being cultured.

Fig. 5 shows the images obtained for beadless freshwater cultured pearl CP-1b. The comma-shaped cavity in the centre of the pearl – a characteristic feature of such beadless cultured pearls – is easily recognized in all images, especially after applying the high pass filter. Drying fissures (indicated by the red arrow) along seasonal growth layers can be seen in the differential phase contrast and scatter dark field images – and also in the absorption image after application of the high pass filter.

Fig. 5 is a good example which shows the particular sensitivity of the scatter dark field image to visualize fine microstructures in pearls, especially when comparing the visibility of the drying fissures in Figs. 5d–5f. In the filtered absorption image (Fig. 5d), only one circular drying fissure can be seen and the signal is very weak. In the differential phase contrast image (Fig. 5e), two fissures are seen but again rather weak. Only the scatter dark field image (Fig. 5f) reveals three distinct drying

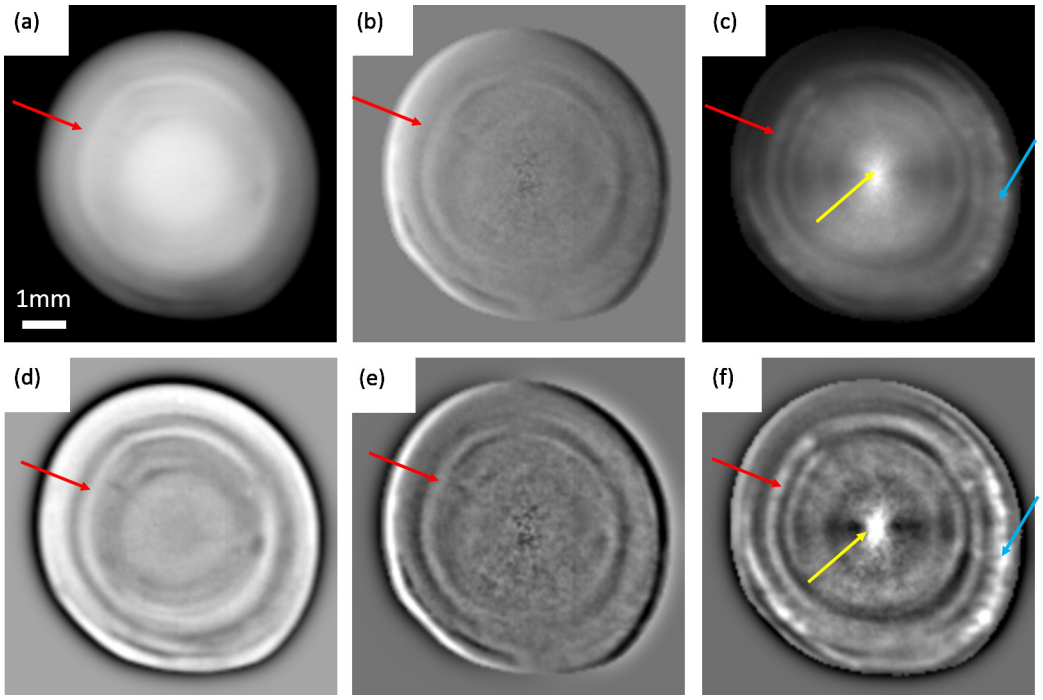

Fig. 3. Images obtained by grating interferometry of the natural pearl NP-2f of the absorption (a), differential phase contrast (b) and scatter dark field (c). (d), (e) and (f) are the images obtained by applying the high pass filter on (a), (b) and (c), respectively.

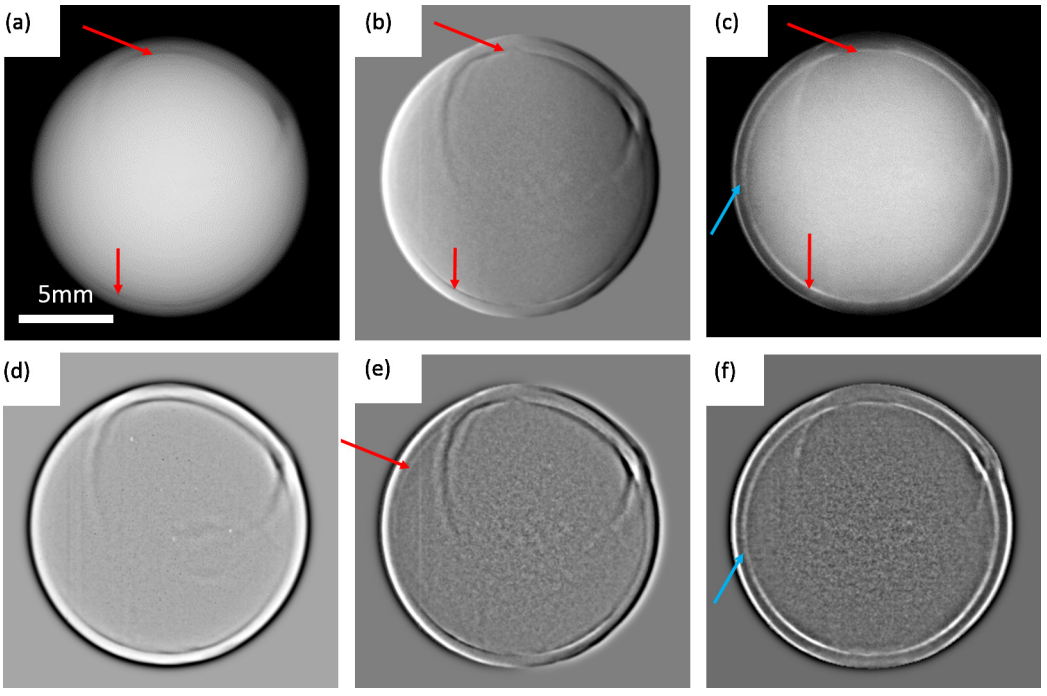

Fig. 4. Images obtained by grating interferometry of the beaded cultured pearl CP-2f of the absorption (a), differential phase contrast (b) and scatter dark field (c). (d), (e) and (f) are the images obtained by applying the high pass filter on (a), (b) and (c), respectively.

fissures. To visualize the effect described above we have plotted the signal intensity for the three filtered images along a line going through the centre of the pearl as shown in Fig. 6. The plots confirm the observations made on the images. Only the scatter dark field signal allows to detect the three fissures clearly. The positions of the fissures are indicated with a dash-dotted line and red arrows in Fig. 6.

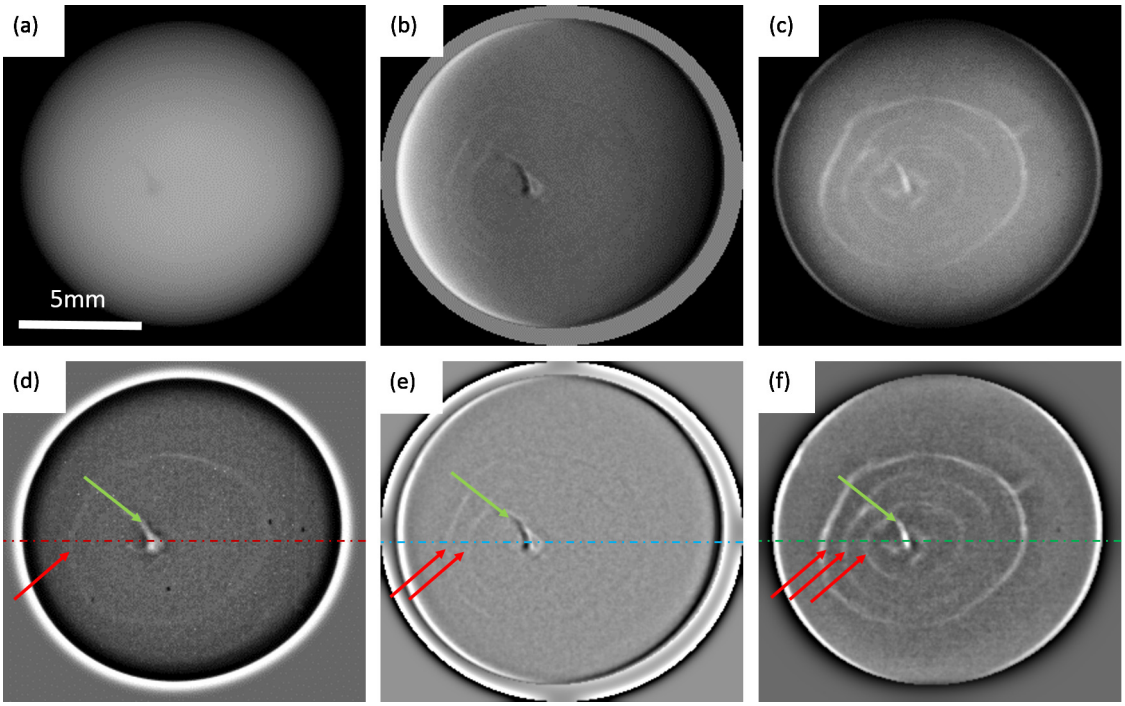

Fig. 5. Images obtained by grating interferometry of the beadless freshwater cultured pearl CP-1b of the absorption (a), differential phase contrast (b) and scatter dark field (c). (d), (e) and (f) are the images obtained by applying the high pass filter on (a), (b) and (c), respectively.

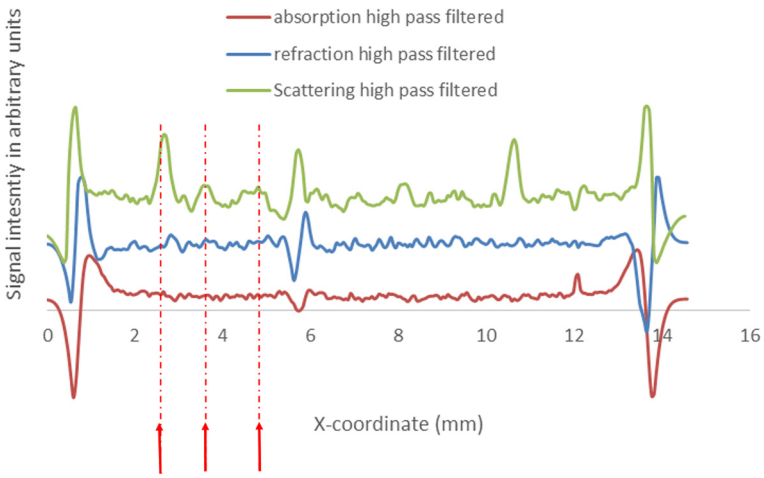

Fig. 6. Plots of the signal intensity of the absorption, differential phase contrast and scatter dark field images along the dotted lines indicated in Fig. 5-def.

4. Discussion

Pearls are a product of biomineralization and may also be understood as calcium carbonate concretions (mainly aragonite and calcite) with small amounts of organic matter (conchioline) interlayered into the carbonate matrix. To be able to safely separate natural pearls from their cultured counterparts, it is absolutely crucial to visualize the internal features using a non-destructive analytical approach. The present study shows, that X-ray phase contrast imaging is adding valuable information complementary to traditional X-ray absorption (radiography). One drawback of conventional radiography is that layers of organic matter and drying fissures are often very thin and irregularly oriented within the spherical volume of the pearl. Thus, the X-ray attenuation difference by these structures is only weak and hardly visible on X-ray films. In contrast to this, X-ray differential phase contrast imaging is especially effective to visualize such tiny structures (compare Fig. 5a and 5b). The differential phase contrast creates a virtual “topographical” image, and clearly reveals the outline of the small comma-shaped cavity (green arrow in Fig. 5b), which is characteristic for a beadless freshwater cultured pearl. With the simultaneously created X-ray scatter dark field image, we even gain further information because of scattering at tiny struc-

tures, such as microfissures (Fig. 3c blue arrow), or nodular areas with increased concentration of organic matter (Fig. 3c yellow arrow). It also improves the visibility of the thin circular organic-rich interlayer between the spherical bead and the on-grown nacre layer of the beaded cultured pearl (Fig. 4c), when compared to its X-ray absorption and even X-ray phase contrast image. The dark field images are also much less affected by the spherical shape of pearls than the absorptio image, thus even fine structures close to the surface are easy to see (compare Fig. 4c with 4a).

In this study, the resulting images were further processed by a high-pass filter. This filter was used to selectively intensify the higher frequencies thus helping to visualize key features present in the studied pearls. The effect of this electronic filter is particularly evident when comparing the absorption images of the natural pearl with and without filter (Fig. 3a and 3d). The filter distinctly enhances the contrast of the layers of alternating X-ray density. Another example is shown in Fig. 5 (images a and d) of the beadless freshwater cultured pearl, revealing that the drying fissures are only discernible after applying this filter. In comparison to this, the filter effect is distinctly less pronounced for the differential phase contrast and scatter dark field images. However, we can still observe an increase of the signal to noise ratio, as for instance between images (c) and (f) in Fig. 4. The interface layer between the bead and the nacre had, however, already been clearly visible in image (c) before filtering.

The present study shows that X-ray scatter dark field images complement conventional X-ray absorption images. They allow to visualize microscopic structures in pearls, which are even below the spatial resolution used for these measurements. Furthermore, the characteristics revealed by the images obtained for CP-2f (bead in Fig. 4) and CP-1b (comma-shaped cavity in Fig. 5) clearly identify them as cultured pearls [7,8]. In contrast to this, NP-2f does not only show a regular, onion-like structure but lacks any indication of an artificial nucleus which therefore allows for it to be classified as natural. Thus, a rapid and efficient separation of natural from cultured pearls was possible with help of X-ray scatter dark field radiography (2D). Still, the interpretation of some structures revealed by scatter dark field imaging remains challenging. First, this is due to the current lack of studies about pearl structures in X-ray scatter dark field images, and second it is due to the limited spatial resolution of the current system.

Based on our experience, it is possible to develop X-ray phase contrast imaging systems with higher spatial resolution (e.g. between 10 to 20 μm). We presume that such an increase in resolution would enable to interpret pearl features more accurately. However, such an increase in spatial resolution would result in a longer exposure time.

Furthermore, X-ray phase contrast imaging can be combined with computed tomography to allow a 3D visualization of the absorption, refraction and scattering coefficients [19,20]. Such 3D information would facilitate the interpretation of the pearl's internal structure but would be obtained at the cost of measurement time. An X-ray phase contrast computed tomography typically takes between 60 to 240 minutes for a single pearl. Contrary to this, the X-ray phase contrast radiography system used in this study can inspect 10 to 20 pearls simultaneously with an exposure time of about 3 minutes. This is a strong advantage compared to standard inspection techniques used today.

5. Conclusions

With this study, the authors show the potential of X-ray phase contrast techniques as a new analytical method for pearl analysis for the first time, especially with regard to the economically relevant separation of natural pearls from cultured ones. Although traditionally based on X-ray radiography and more recently on X-ray microtomography, our results reveal that X-ray phase contrast – in particular scatter dark field imaging – is a promising method to visualize internal features in pearls in great detail and distinctly faster than most traditional pearl analysis techniques.

Acknowledgement

The authors acknowledge the funding from the European Union's Seventh Framework Programme for research technological development and demonstration under grant agreement n° 314735. We would also like to thank Philippe Niedermann and Jacek Baborowski from CSEM for helping with the fabrication of the X-ray gratings.

References

[1] Simkiss K, Wada K. Cultured pearls – commercialised biomineralisation. Endeavour 1980;4:32–7.
[2] Strack E. Pearls. Rühle-Diebener Verlag; 2006.
[3] Southgate P, Lucas J. The pearl oyster. 1st ed. 2008.
[4] Hänni HA. Natural pearls and cultured pearls: a basic concept and its variations. Aust Gemmol 2012;24:256–66.
[5] Christie's. La Peregrina: a natural pearl, diamond, ruby and cultured pearlnecklace, by Cartier 2011. http://www.christies.com/lotfinder/jewelry/la-peregrina-a-natural-pearl-diamond-5507887-details.aspx.
[6] Anderson BW. The use of X rays in the study of pearls. Br J Radiol 1932;5:57–64. http://dx.doi.org/10.1259/0007-1285-5-49-57.
[7] Wehrmeister U, Goetz H, Jacob DE, Soldati AL, Xu W, Duschner H, et al. Visualization of the internal structure of freshwater cultured pearls by computerized X-ray microtomography. J Gemmol 2008;32:15–21.
[8] Krzemnicki MS, Friess SD, Chalus P, Hänni HA, Karampelas S. X-ray computed microtomography: distinguishing natural pearls from beaded and non-beaded cultured pearls. Gems Gemol 2010;46:128–34.
[9] David C, Nöhammer B, Solak HH, Ziegler E. Differential x-ray phase contrast imaging using a shearing interferometer. Appl Phys Lett 2002;81:3287. http://dx.doi.org/10.1063/1.1516611.
[10] Momose A, Kawamoto S, Koyama I, Hamaishi Y, Takai K, Suzuki Y. Demonstration of X-ray Talbot interferometry. Jpn J Appl Phys 2003;42:L866–8. http://dx.doi.org/10.1143/JJAP.42.L866.

[11] Pfeiffer F, Weitkamp T, Bunk O, David C. Phase retrieval and differential phase-contrast imaging with low-brilliance X-ray sources. Nat Phys 2006;2:258–61. http://dx.doi.org/10.1038/nphys265.
[12] Revol V, Kottler C, Kaufmann R, Jerjen I, Lüthi T, Cardot F, et al. X-ray interferometer with bent gratings: towards larger fields of view. Nucl Instrum Methods Phys Res, Sect A, Accel Spectrom Detect Assoc Equip 2011;648:S302–5. http://dx.doi.org/10.1016/j.nima.2010.11.040.
[13] Revol V, Kottler C, Kaufmann R, Straumann U, Urban C. Noise analysis of grating-based x-ray differential phase contrast imaging. Rev Sci Instrum 2010;81:73709. http://dx.doi.org/10.1063/1.3465334.
[14] Revol V, Jerjen I, Kottler C, Schütz P, Kaufmann R, Lüthi T, et al. Sub-pixel porosity revealed by x-ray scatter dark field imaging. J Appl Phys 2011;110:44912. http://dx.doi.org/10.1063/1.3624592.
[15] Pfeiffer F, Bech M, Bunk O, Kraft P, Eikenberry EF, Brönnimann C, et al. Hard-X-ray dark-field imaging using a grating interferometer. Nat Mater 2008;7:134–7. http://dx.doi.org/10.1038/nmat2096.
[16] Weitkamp T, Diaz A, David C. X-ray phase imaging with a grating interferometer. Opt Express 2005;13:6296–304.
[17] Yashiro W, Terui Y, Kawabata K, Momose A. On the origin of visibility contrast in x-ray Talbot interferometry. Opt Express 2010;18:16890–901.
[18] ImageJ. http://rsb.info.nih.gov/ij/index.html. n.d.
[19] Herzen J, Donath T, Pfeiffer F, Bunk O, Padeste C, Beckmann F, et al. Quantitative phase-contrast tomography of a liquid phantom using a conventional x-ray tube source Abstract. Opt Express 2009;17:622–8.
[20] Kottler C, Revol V, Kaufmann R, Niedermann P, Cardot F, Dommann A. X-ray grating-based phase contrast CT for non-destructive testing and evaluation. In: Int Conf Ind Comput Tomogr, vol. 1. 2012. p. 129–34.